

# 3D Lattice Boltzmann Simulation of Droplet Evaporation on Patterned Surfaces: Study of Pinning-Depinning Mechanism

Boheng Dong<sup>a, †</sup>, Fuxian Wang<sup>b, †</sup>, Xinya Zhang<sup>a</sup>, Xiang Jiang<sup>a, \*</sup>

<sup>a</sup> Key Laboratory of Enhanced Heat Transfer and Energy Conservation of Education Ministry, School of Chemistry and Chemical Engineering, South China University of Technology, Guangzhou 510640, China

<sup>b</sup> Guangdong Provincial Key Laboratory of Emergency Test for Dangerous Chemicals, Guangdong Institute of Analysis, Guangzhou 510070, China

**KEYWORDS:** Pinning-depinning, Evaporation, Chemically stripe-patterned surfaces, Lattice Boltzmann

**ABSTRACT:** The liquid-vapor phase change lattice Boltzmann method is used to investigate the pinning-depinning mechanism of the contact line during droplet evaporation on the stripe-patterned surfaces in 3D space. Considering the curvature of the contact line and the direction of the unbalanced Young's force, the local force balance theory near the stripe boundary is proposed to explain the steady state of the droplets on the stripe-patterned surfaces. An equation is proposed to evaluate the characteristic contact angle of the stabilized droplets. During the evaporation of the droplet, the stick-slip-jump behavior and the CCR-Mixed-CCA mode can be well captured by the lattice Boltzmann simulation. When the contact line is pinned to the stripe boundary, the contact line in the direction perpendicular to the stripes is slowly moving while the curvature of the contact line is gradually increasing. The gradually increasing curvature of the contact line accelerates the movement of the contact line, and the final contact line is detached from the stripe boundary. The research results provide theoretical support and guidance for the design, improvement and application of patterned surfaces in the field of micro-fluidic and evaporation heat transfer.

## 1. INTRODUCTION

Evaporation of the droplet is not only a ubiquitous phenomenon in nature but also a process that is widely used in many engineering fields, such as inkjet printing[1-2], spray cooling[3], thin film coating[4-5] and chip manufacturing[6-7]. Surface properties, such as material, roughness and wettability, affect the distribution of the droplets on the surface and the movement of the contact line during evaporation. Studies have shown that the patterned surfaces exhibit superior performance in heat and mass transfer compared to the uniform surfaces[8-12]. Therefore, in-depth study of the internal mechanism of the droplet evaporation on the patterned surfaces is of great importance for the design and engineering application of patterned surfaces.

In recent years, tremendous research efforts have been made in investigating the pinning-depinning mechanism[13-18] on patterned surfaces, such as structurally rough surfaces[19-23] and chemically heterogeneous surfaces[24-29]. The pinning and depinning forces[20, 30] and the intrinsic energy barrier [23, 31] were used to explain the pinning-depinning mechanism. The pinning-depinning process is accompanied by changes in contact angle and contact radius. The constant contact radius (CCR) mode, the constant contact angle (CCA) mode[32], and the mixed mode[33-36] were developed to explain the pinning-depinning mechanisms. Researchers found that the contact angle of the droplet on chemically patterned surface is determined by the solid-liquid interaction on the three-phase contact line [15-16, 22, 37-38] rather than the whole contact surface as described in Cassie equations [39]. Based on the solid-liquid interaction on the three-phase contact line, the local force balance theories were proposed to explain the pinning-depinning mechanism of the droplet evaporation on chemically

patterned surface and the local Cassie equations were formulated to predict the contact angle variations both in equilibrium and in evaporation situations[15-16]. However, the local force balance theories and local Cassie equations were proposed only on the basis of 2D research. Considering that in practical the droplet evaporation occurs in 3D, so 3D studies are essential for real application, especially for droplet evaporation on droplet evaporation patterned surfaces.

In this work, we simulate the phenomenon of 3D droplet evaporation on chemically stripe-patterned surfaces using lattice Boltzmann method (LBM). An equation is proposed to predict the characteristic contact angle by analyzing the local force near the stripe boundary. The local force balance theory near the stripe boundary is used to explain the pinning-depinning mechanism during 3D droplet evaporation. This work presents new understanding of the pinning-depinning behavior of the contact line and provides theoretical support for the design, improvement, and practical application of patterned surfaces for evaporation heat transfer.

## 2. NUMERICAL MODEL

In this paper, the modified pseudo-potential phase change model based on Gong and Cheng[40-42] is used to simulate droplet evaporation on stripe-patterned surface.

### 2.1 The Modified Pseudo-Potential Lattice Boltzmann Model

Lattice Boltzmann proceeds by a sequence of collision and stream steps. The fluid is described by the evolution of microscopic fluid particles and particle distribution function. The density distribution function of the S-C model with the BGK collision operator is governed by

$$f_i(x + e_i \delta_t, t + \delta_t) - f_i(x, t) = -\frac{1}{\tau} (f_i(x, t) - f_i^{eq}(x, t)) + \Delta f_i(x, t) \quad (1)$$

where  $f_i(x, t)$  and  $f_i^{eq}(x, t)$  are the density distribution function and the equilibrium distribution with velocity  $e_i$  at position  $x$  and time  $t$ , respectively.  $\Delta f_i(x, t)$  is the body force term,  $\tau$  is the relaxation time,  $f_i^{eq}(x, t)$  are given by

$$f_i^{eq}(x, t) = \omega_i \rho \left[ 1 + \frac{e_i \cdot u}{c_s^2} + \frac{(e_i \cdot u)^2}{2c_s^4} - \frac{u^2}{2c_s^2} \right] \quad (2)$$

and  $\Delta f_i(x, t)$  are given by

$$\Delta f_i(x, t) = f_i^{eq}(\rho(x, t), u + \Delta u) - f_i^{eq}(\rho(x, t), u) \quad (3)$$

where  $\Delta u = F \delta_t / \rho$  is the velocity change under the action of body force during time step  $\delta_t$ .

$$F = F_{int}(x) + F_g(x) + F_s(x) \quad (4)$$

where the  $F_{int}$ ,  $F_g$  and  $F_s$  are the interparticle interaction force, gravitation force and interaction force between solid and fluid, respectively.  $F_{int}$  is given by

$$F_{int}(x) = -\beta \psi(x) \sum_{x'} G(x, x') \psi(x') (x + x') - \frac{1-\beta}{2} \sum_{x'} G(x, x') \psi^2(x') (x + x') \quad (5)$$

where  $\psi(x)$  is the "effective mass" given by

$$\psi(x) = \sqrt{\frac{2(p - \rho c_s^2)}{c_0 G}} \quad (6)$$

with  $c_0 = 6.0$  for the D3Q19 scheme.  $G(x, x')$  is given by

$$G(x, x') = \begin{cases} G_1, & |x + x'| = 1 \\ G_2, & |x + x'| = \sqrt{2} \\ 0, & \text{otherwise} \end{cases} \quad (7)$$

with  $G_1 = G$ ,  $G_2 = G/2$  for D3Q19 scheme.

In this model, the P-R EOS (equation of state) will be adopted, which is given by

$$p = \frac{\rho RT}{1 - b\rho} - \frac{a\rho^2 \varepsilon(T)}{1 + 2b\rho - b^2\rho^2} \quad (8)$$

where  $a = 0.45724R^2 T_{cr}^2 / p_{cr}$ ,  $b = 0.0778R T_{cr} / p_{cr}$ ,

$$\varepsilon(T) = \left( 1 + \left( 1 - \sqrt{T/T_{cr}} \right) (0.37464 + 1.54226\omega - 0.266992\omega^2) \right)^2 \quad (9)$$

$T_{cr}$  and  $p_{cr}$  represent critical temperature and critical pressure. In this paper, we set  $a = 2/49$ , and  $b = 2/21$ ,  $R = 1$  and  $\omega = 0.344$ .

The gravitation force  $F_g$  is given by

$$F_g(x) = G \cdot (\rho(x) - \rho_{ave}) \quad (10)$$

where  $G$  is the acceleration of gravity and  $\rho_{ave}$  is the average density of the whole computation domain at each time step. Interaction force  $F_s$  between solid and fluid is given by

$$F_s(x) = -\psi(x) \sum_i G_s \omega_i s(x + e_i \delta_t) \cdot e_i \delta_t \quad (11)$$

where  $G_s$  is the interaction strength between fluid and solid, which is used to adjust the contact angle.  $s(x)$  is the indicator function when  $x$  is in solid which is equal to 1 and when  $x$  is in fluid which is equal to 0.

In this paper, the D3Q19 scheme is chosen for 3D simulations. The weighting coefficients  $\omega_i$  and the discrete velocity vectors  $e_i$  are given by

$$\omega_i = \begin{cases} 1/3 & i = 0 \\ 1/18 & i = 1 - 6 \\ 1/36 & i = 7 - 18 \end{cases} \quad e_i = \begin{cases} (0,0,0) & i = 0 \\ (\pm 1, 0, 0)c, (0, \pm 1, 0)c, (0, 0, \pm 1)c & i = 1 - 6 \\ (\pm 1, \pm 1, 0)c, (\pm 1, 0, \pm 1)c, (0, \pm 1, \pm 1)c & i = 7 - 18 \end{cases}$$

For D3Q19 schemes  $c_s^2 = c^2/3 = 1/3$ . The kinematic viscosity can be adjusted by changing the relaxation time which is given by

$$\nu = c_s^2(\tau - 1/2)\delta_t \quad (12)$$

The density and velocity of the fluid can be obtained by

$$\rho = \sum_i f_i, \quad \rho u = \sum_i e_i f_i \quad (13)$$

Note that  $u$  in Eq. (2) and Eq. (3) is not the real fluid velocity. The real fluid velocity  $U$  is given by

$$\rho U = \rho u + (\delta_t/2)F \quad (14)$$

## 2.2 Energy Equation Model and Derivation of The Source Term

The temperature distribution function for the energy equation model is given by

$$g_i(x + e_i \delta_t, t + \delta_t) - g_i(x, t) = -\frac{1}{\tau_T} (g_i(x, t) - g_i^{eq}(x, t)) + \delta_t \omega_i \phi \quad (15)$$

where  $\phi$  is the source term given by

$$\phi = T \left( 1 - \frac{1}{\rho c_v} \left( \frac{\partial p}{\partial T} \right)_\rho \right) \nabla \cdot U + \frac{\nabla \cdot (k \nabla T)}{\rho c_v} - \nabla \cdot (\alpha \nabla T) \quad (16)$$

with  $\alpha$  being the thermal diffusivity which is given by  $\alpha = k/(\rho c_p)$ . The equilibrium distribution function for temperature is given by

$$g_i^{eq}(x, t) = \omega_i T \left[ 1 + \frac{e_i \cdot U}{c_s^2} + \frac{(e_i \cdot U)^2}{2c_s^4} - \frac{U^2}{2c_s^2} \right] \quad (17)$$

The D3Q19 scheme is chosen for the computation of temperature. Hence the thermal diffusivity is given by

$$\alpha = c_s^2(\tau_T - 1/2)\delta_t \quad (18)$$

The temperature is given by

$$T = \sum_i g_i \quad (19)$$

Note that there is a density gradient at the liquid-vapor interface. Thus, other fluid properties  $\chi$  (such as  $\nu$  and  $\alpha$ ) are given by

$$\chi = \chi_l \cdot \frac{\rho - \rho_v}{\rho_l - \rho_v} + \chi_v \cdot \frac{\rho_l - \rho}{\rho_l - \rho_v} \quad (20)$$

where  $\rho_l$  and  $\rho_v$  are densities of the saturated liquid and saturated of vapor, respectively.

## 3. NUMERICAL RESULTS AND DISCUSSION

### 3.1 Spreading of Droplets on The Stripe-Patterned Surface Without Evaporation

The chemically stripe-patterned surfaces are illustrated in figure 1, where the dark (A) and light (B) stripes represent the hydrophilic and hydrophobic area, respectively.  $\theta_A$  and  $\theta_B$  are the equilibrium contact angle of stripes A and stripes B ( $\theta_A = 65^\circ$ ,  $\theta_B = 131^\circ$ ). The hydrophilic and hydrophobic stripes have the same width.  $W_x$  and  $W_y$  are the maximum contact lengths of the droplets in the X and Y directions, respectively.  $H$  is the maximum height of the droplet.

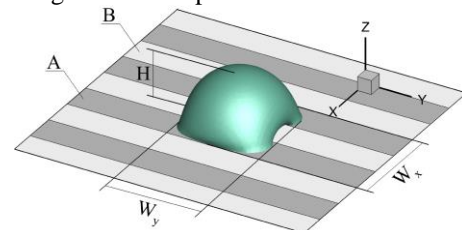


**Fig 1.** Stable droplets on chemically stripe-patterned surfaces; A: hydrophilic stripes; B: hydrophobic stripes;  $W_x$ : maximum contact length in the X direction;  $W_y$ : maximum contact length in the Y direction.

The simulation works are carried out in a three-dimensional cuboid domain  $L_x \times L_y \times L_z = 100 \times 100 \times 80$  lattice units (lu for short). The stripe width is set to 9 lu, 11 lu, 13 lu and 15 lu, and the corresponding stripe-patterned surfaces are named  $W_9$ ,  $W_{11}$ ,  $W_{13}$  and  $W_{15}$ , respectively. The half-way bounce-back scheme is applied at the lower boundary (solid wall). The open boundary condition is applied at the upper boundary, and the periodic boundary condition is employed at all other boundaries. Initially, a hemispherical droplet of radius  $R_0 = 20(\text{lu})$  is deposited on the chemically stripe-patterned surface. The kinematic viscosity of saturated liquid phase and saturated vapor phase are taken as  $\mu_l = 0.354$  and  $\mu_v = 0.0348$ . Other properties are set to be: thermal diffusivity  $\alpha_l = 0.05$  and  $\alpha_v = 0.06$ , specific heat  $c_{p,l} = c_{v,l} = 4.0$  and  $c_{p,v} = c_{v,v} = 4.0$ , Prandtl numbers  $Pr_l = 1.2$  and  $Pr_v = 1.0$ , where subscripts  $l$  and  $v$  represent liquid and vapor, respectively.

This section discusses in detail the effects of the initial position of the droplet and the width of the stripe on the dynamic spreading of the droplets on a patterned surface. There are two cases of the initial position of the droplet. Case 1: The centroid of the droplet is located in the middle of a hydrophilic stripe (Figure 2(a)). Case 2: The centroid of the droplet is located in the middle of a hydrophobic stripe (Figure 2(b)). In Li et al.'s [15] study, Case 1 was selected whereas in Zhang et al.'s [16] study, Case 2 was selected. In this work, both cases are simulated and analysis in theory is discussed.

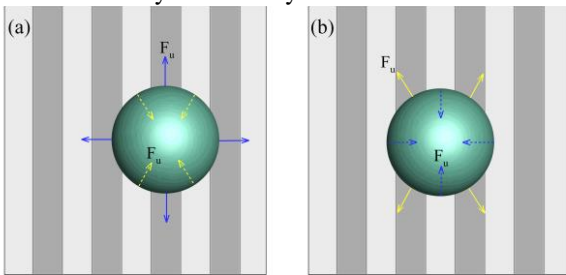


**Fig 2.** Initial position of the droplet on the  $W_{11}$ : (a) Centered on hydrophilic stripe, (b) Centered on hydrophobic stripe.

In theory, if the centroid of the droplet just is located in the middle of the stripes, the droplet can reach a steady state at the initial position. However, in reality, it is almost impossible to be realized, because there are always unobservable disturbances in the actual situations. Hence, we add an “artificial disturbance” to the simulation calculation. In the initial state, the centroid of the droplet deviates slightly from the middle of stripes (0.2 lu). For Case 1, the process of the droplet on the  $W_{11}$  from the initial state to the steady state is shown in Figure 3. In the initial stage ( $t=0 \sim 500 \delta_t$ ), the droplet spreads rapidly along the X-axis under the influence of the hydrophilic stripes. When  $t=500 \sim 1000 \delta_t$ , the droplet is asymmetrically distributed. The centroid and contact line move to the right. When  $t=1000 \sim 2000 \delta_t$ , the right contact line is completely detached from the hydrophilic stripe. After detachment, the right contact line quickly skips the hydrophobic stripes. When  $t=2000 \sim 6000 \delta_t$ , the droplet reaches a steady state gradually. Eventually, the droplet covers three stripes with one hydrophobic stripe in the middle and two hydrophilic stripes on the left and right. For Case 2, the steady state of the droplet is the same as in Case 1, but Case 2 takes less time to stabilize than Case 1 since the initial state of Case 2 is closer to the steady state.

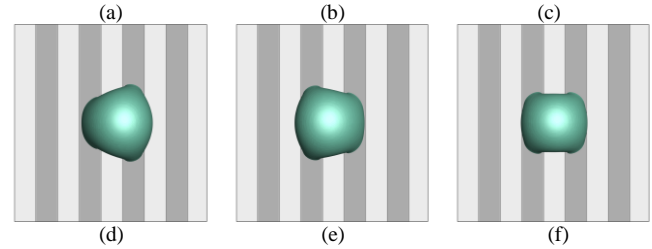
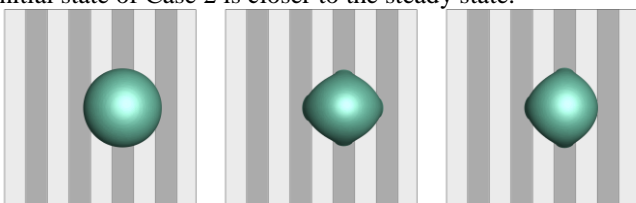


**Fig 3.** The process of droplet spreading on the  $W_{11}$  surface: (a)  $t=0 \delta_t$ , (b)  $t=500 \delta_t$ , (c)  $t=1000 \delta_t$ , (d)  $t=2000 \delta_t$ , (e)  $t=3000 \delta_t$  and (f)  $t=6000 \delta_t$ .

The asymmetric migration similar to Case 2 is also found in the study of Zhang et al. [16]. This phenomenon can be explained from the perspective of the force balance on the contact line. Since the shape of the initial droplet is hemispherical with an initial contact angle  $\theta$  of  $90^\circ$ . The contact angle  $\theta$  deviates from the equilibrium contact angle of hydrophilic stripes and hydrophobic stripes,  $\theta_A < \theta < \theta_B$ , so an unbalanced Young's force (per unit length) can be defined [43] as:

$$F_u = \gamma(\cos \theta - \cos \theta_e) \quad (21)$$

where  $\gamma$  is surface tension,  $\theta$  and  $\theta_e$  are arbitrary contact angle and equilibrium contact angle, respectively. Figure 2(a) and (b) show the unbalanced Young's force acting on the contact line. On the hydrophilic stripes, the direction of the force is toward the outside of the droplet, so the droplet tends to spread. However, on the hydrophobic stripes, the direction of the force is toward the inside of the droplet, so the droplet tends to shrink. The “artificial disturbance” breaks the force balance and causes an asymmetric migration of the droplet. From the simulation results, it can be seen that the droplet in Case 2 is more stable than that in Case 1. Firstly, this is related to the area ratio of hydrophilic and hydrophobic stripes occupied by the solid-liquid contact surface). The droplet spreads sufficiently on the hydrophilic strip and has a lower center of gravity. The larger the area ratio of the hydrophilic stripes increases the stability of the droplet. Secondly, this is also related to the stripe boundary. There are two types of stripe boundary, one is the boundary from A (hydrophilic) to B (hydrophobic) and the other is the boundary from B to A, in the direction pointing to the center of the droplet. The research shows that the contact line can be pinned at the B to A boundary but not at the A to B boundary. For Case 2, the area ratio of the hydrophilic stripes is larger than Case 1 and the B to A boundary at both sides of the droplet can easily capture the contact line. Therefore, in the following discussions, the Case 2 is the default initial state of the droplet.

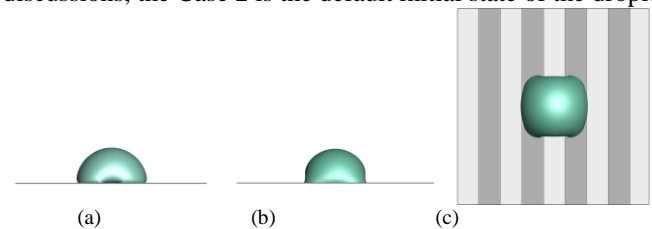


**Fig 4.** Three views of the droplets in the steady state: (a) Front view, (b) left view and (c) top view.

From Figure 4 it can be seen that the contact line on the chemically stripe-patterned surface is an irregular closed curve. In the Y-axis direction, the droplet spreads on the hydrophilic stripes and shrinks on the hydrophobic stripe. Therefore, the droplet contact angle is small and the contact line is convex on the hydrophilic stripes and the contact angle of the droplet is large and the contact line is concave on the hydrophobic stripe. In the X-axis direction, the contact lines cannot spread more and cling to the stripe boundary, under the influence of the B to A boundary. By introducing parameters  $W_x$ ,  $W_y$ ,  $H$  and  $\theta_c$ , the quantitative analysis of the droplet evaporation process can be

performed more accurately.  $\theta_c$ , the “characteristic contact angle”, is defined as the average contact angle of the droplet’s projected in the Y direction (see Figure 4(a)).

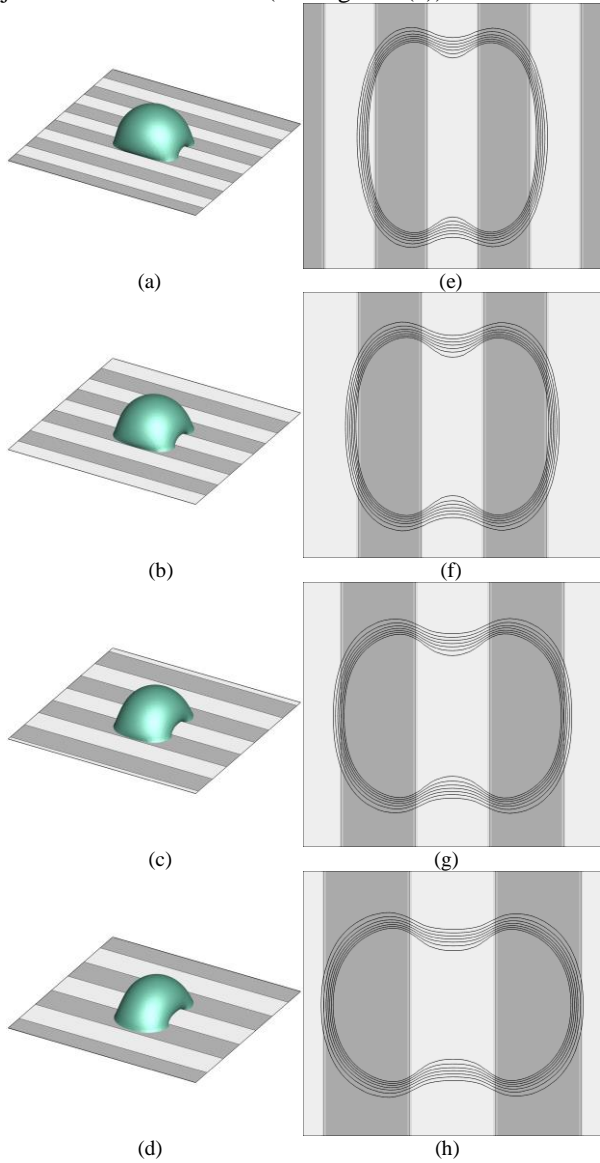


**Fig 5.** (a-d) Steady states of droplets on  $W_9$ ,  $W_{11}$ ,  $W_{13}$  and  $W_{15}$  surfaces, (e-h) The liquid-vapor interfaces at the contact line.

Steady states of the droplets on different surfaces are displayed in Figure 5a-d. The figure clearly shows that the width of the stripe has a large effect on the shape characteristics of the droplets. As the stripe width increases,  $W_x$  increases,  $W_y$  and  $\theta_c$  decrease. Characteristic contact angle  $\theta_c$  are 129.4°, 117.9°, 93.5° and 73.7°, respectively. It should be noted that in fact the liquid-vapor interfaces are a region with a finite width and there is a density gradient on the interfaces. Taking into consideration the thickness of liquid-vapor interfaces, the three-phase contact line can be denoted by several iso-density lines as shown in Figure 5e-h. The iso-density lines on the hydrophobic stripes are slightly sparse than the iso-density lines on the hydrophilic stripes. From the simulation results, it can be found that the characteristic contact angles  $\theta_c$  is varies with the position of the contact line near the stripe boundary. The contact angle of the droplet on chemically patterned surface is determined by the solid-liquid interaction on the three-phase contact line. Li et al.[15] analyzes the local force balance in the diffuse interfaces and proposed the following equation

$$\cos \theta = l_A \cos \theta_A + l_B \cos \theta_B \quad (22)$$

where  $\theta$  is the characteristic contact angle of the droplets on chemically stripe-patterned surfaces,  $l_A$  and  $l_B$  are the length ratios of the contact line occupied by components A and B.

However, this equation applies only to the 2D droplet. In 3D space, the curvature of the contact line and the direction of unbalanced Young’s force must be considered.

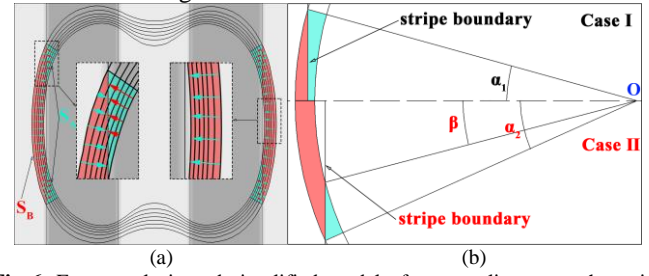


**Fig 6.** Force analysis and simplified model of contact lines near the stripe boundary ( $W_{11}$  surfaces): (a) Force analysis, (b) Simplified model.

As shown in Figure 6a, part of the contact line near the stripe boundary is sitting on the hydrophilic stripe ( $S_A$ ) while the other part is sitting on the hydrophobic stripe ( $S_B$ ). The direction of unbalanced Young’s force is perpendicular to the contact line, so the direction of the force at different locations is different. Therefore, in order to make the calculation simple, the model is simplified, as shown in Figure 6b. Suppose that the contact line near the stripe boundary is composed of two concentric arcs. The central angle of the arc is  $2\alpha$ . The radius of the two concentric arcs are  $R$  and  $r$ , respectively. The distance from the stripe boundary to the center of the circle is  $L$ . There are two cases, one is  $R > L > r$  (Case I) and the other is  $R > r > L$  (Case II). The local force balance (X-axis direction) at contact lines near stripe boundary can be formulated as follows

$$S'_A \gamma (\cos \theta_c - \cos \theta_A) = -S'_B \gamma (\cos \theta_c - \cos \theta_B) \quad (23)$$

where  $S'_A$  and  $S'_B$  are the X-axis direction “effective area” of contact line occupied by stripe A and B, respectively. In polar coordinates, contact line and stripe boundary can be obtained

$$\begin{cases} \rho_1(\theta) = R & (-\alpha < \theta < \alpha) \\ \rho_2(\theta) = r & (-\alpha < \theta < \alpha) \\ \rho_3(\theta) = L/\cos \theta & (-\alpha < \theta < \alpha) \end{cases} \quad (24)$$

For Case I, the X-axis direction “effective area” of the contact line can be obtained

$$S'_A = 2 \int_0^\alpha \cos \theta \left[ \frac{1}{2} \rho_3(\theta)^2 - \frac{1}{2} \rho_2(\theta)^2 \right] d\theta \quad (25)$$

$$S'_B = 2 \int_0^\alpha \cos \theta \left[ \frac{1}{2} \rho_1(\theta)^2 - \frac{1}{2} \rho_3(\theta)^2 \right] d\theta \quad (26)$$

and for Case II

$$S'_A = 2 \int_\beta^\alpha \cos \theta \left[ \frac{1}{2} \rho_3(\theta)^2 - \frac{1}{2} \rho_2(\theta)^2 \right] d\theta \quad (27)$$

$$S'_B = 2 \int_\beta^\alpha \cos \theta \left[ \frac{1}{2} \rho_1(\theta)^2 - \frac{1}{2} \rho_3(\theta)^2 \right] d\theta + 2 \int_0^\beta \cos \theta \left[ \frac{1}{2} \rho_1(\theta)^2 - \frac{1}{2} \rho_2(\theta)^2 \right] d\theta \quad (28)$$

It should be noted that  $\int \frac{1}{2} \rho(\theta)^2 d\theta$  is real area and  $\int \frac{1}{2} \cos \theta \rho(\theta)^2 d\theta$  is “effective area” (X-axis direction), where the direction of the force is considered. Make  $s'_A = S'_A / (S'_A + S'_B)$  and  $s'_B = S'_B / (S'_A + S'_B)$ , the prediction equation can be obtained

$$\cos \theta_c = s'_A \cos \theta_A + s'_B \cos \theta_B \quad (29)$$

**Table 1.** Predicted results and errors of Eq. (29)

Surface	$s'_A/\%$	$s'_B/\%$	Numerical results	Predicted results	Errors/%
$W_9$	12.0	88.0	129.4°	121.8°	5.87
$W_{11}$	23.7	76.3	117.9°	113.6°	3.65
$W_{13}$	50.5	49.5	93.5°	96.4°	3.10
$W_{15}$	85.6	14.4	73.7°	74.5°	1.09

According to the simulation results,  $s'_A$  and  $s'_B$  can be obtained and then the contact angle can be predicted using Eq. (29) as shown in Table 1. Obviously, the predicted results are in good agreement with the numerical results.

### 3.2 Dynamic Behavior and Pinning-Depinning Mechanism of Evaporating Droplet

The dynamic behavior of evaporating droplet on the stripe-patterned surfaces is studied in this section. At  $t=5000 \delta_t$ , the droplet has reached a steady state without evaporation. The droplet begins to evaporate due to the addition of temperature solver and the temperature of the solid wall is set to  $T_w = 0.9T_c$ , where  $T_c$  is critical temperature. As shown in Figure 7, the droplet gradually evaporates from the  $W_{11}$  surface. The figure displays the variations of  $\theta_c$ ,  $W_x$ ,  $W_y$ , and  $H$  with respect to time. From this figure, we can see that the droplet evaporation is divided into several stages. In stage I, the droplet evaporates in CCR mode. The contact line in X-axis direction is stuck on the B to A boundary (constant  $W_x$ ) and the characteristic contact angle  $\theta_c$  is constantly decreasing. In stage II, the evaporation turns to the mixed mode. The contact line in X-axis direction begins to slowly slip (decreasing  $W_x$ ) and  $\theta_c$  gradually decreases. In stage III, the droplet evaporates in CCA mode.  $\theta_c$  remains constant and the slip of the contact line in X-direction is accelerated. In stages I-III,  $W_y$  and  $H$  continue to decrease. This means that the contact line in Y-axis direction is always slipping.

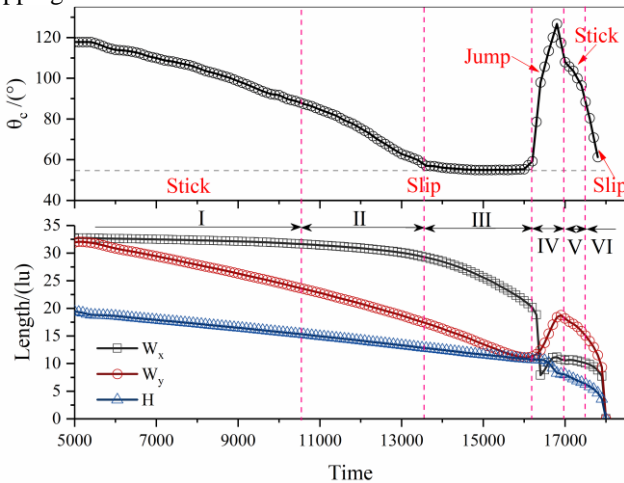


**Fig 7.** Droplet evaporation on the  $W_{11}$  surface and time evolutions of the  $\theta_c$ ,  $W_x$ ,  $W_y$ , and  $H$ .

As the contact line continues to slip, the area of the hydrophilic stripes covered by the droplets decreases, resulting in a decrease in droplet stability. Finally, sudden jump and asymmetric migration occur when the contact line in X-axis direction is near the boundary ( $t \approx 16200 \delta_t$ ), as shown in Figure 8. When  $t=15800 \delta_t$ , the droplet is symmetrically distributed. However, soon the contact line on the right side of the droplet begins to slip rapidly ( $t=15800 \sim 16200 \delta_t$ ). Under a large unbalanced Young's force, the droplet quickly "jump" over the A to B boundary and the hydrophobic stripe ( $t=16200 \sim 16600 \delta_t$ ). Finally, the droplets adhere to the hydrophilic stripe ( $t=17000 \delta_t$ ). In stage IV,  $W_x$  suddenly decreases,  $W_y$  suddenly increases and  $H$  slightly increases and then decreases. This corresponds to the process shown in Figure 8. This phenomenon has a similar principle to the asymmetric migration during droplet spreading. Both are due to the area of the hydrophilic strips covered by the left and right sides of the droplet is too small. Unobservable disturbances break the balance of forces and cause asymmetric migration.

In stage V, the droplet evaporates on the hydrophilic stripe in CCR mode. Since the volume of the droplet is very small, the evaporation goes to the mixed mode quickly and the droplet completely evaporates in a short time (stage VI).

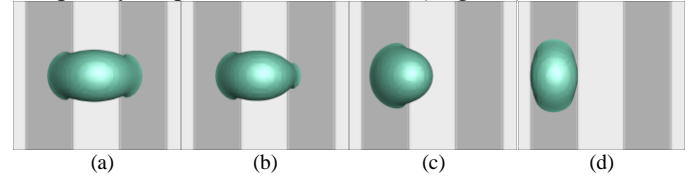


**Fig 8.** Sudden jump and asymmetric migration of the droplet on the  $W_{11}$  surface (stage IV): (a)  $t=15800 \delta_t$ , (b)  $t=16200 \delta_t$ , (c)  $t=16600 \delta_t$  and (d)  $t=17000 \delta_t$ .

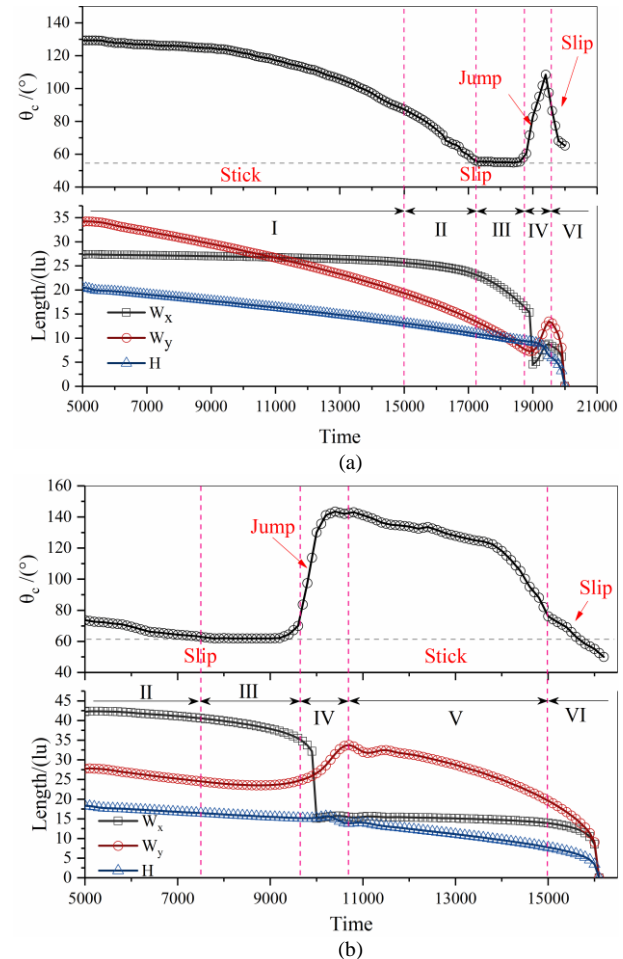


**Fig 9.** Droplet evaporation on  $W_9$  and  $W_{15}$  surfaces and Time evolutions of the  $\theta_c$ ,  $W_x$ ,  $W_y$ , and  $H$ : (a)  $W_9$  surface, (b)  $W_{15}$  surface.

As shown in Figures 9a and 9b, the droplets gradually evaporate from the  $W_9$  and  $W_{15}$  surface, respectively. In these two cases, similar dynamic behavior (stick-slip-jump) can be clearly observed. The main difference compared to  $W_{11}$  is that  $W_9$  and  $W_{15}$  lack a certain stage. Figure 8a clearly shows that the V stage is missing for  $W_9$ . Since the stripe width of the  $W_9$  surface is narrow, the volume of the remaining droplets after stage IV is too small to allow the contact line to be stuck on the stripe boundary. Figure 8b clearly shows that stage I is missing for  $W_{15}$ . Since the stripe width of the  $W_{15}$  surface is wide, the contact line in the X-axis direction hardly contacts the B to A boundary. Therefore, the contact line is not stuck at the B-A boundary but directly slips.

Comparing Figures 7 and 9, it can be seen that the total evaporation time on  $W_9$ ,  $W_{11}$  and  $W_{15}$  surfaces decreases with the width of the stripe. This is because the contact area between the droplet and the surface increases with the width of the stripe. The larger contact area allows for more efficient heat transfer between the droplet and the surface which accelerates the evaporation of the droplet. In addition, we notice that the time

spent on the same stage is also very different when droplets evaporate on different surfaces. For example, the time of stage V on  $W_{15}$  surface is much longer than the time of stage V on  $W_{11}$ . This is still related to the width of the stripe. The wider stripe width causes the droplet to jump earlier. At this time, the volume of the droplet is still large, so the droplet takes longer to completely evaporate from the surface.

The aforementioned contents show the dynamic behavior of evaporating droplet on chemically stripe-patterned, including the pinning-depinning (stages I-III and V-VI). The local force balance theory near the boundary of the stripe has provided a theoretical basis for analyzing the pinning-depinning mechanism. Figure 10 displays the local details of the liquid-vapor interfaces on the  $W_{11}$  surface at  $t=8000 \delta_t$ ,  $10000 \delta_t$  and  $12000 \delta_t$ . The figure clearly shows the contact line in X-axis direction slowly moves toward the center of the droplet. As compared with  $W_x$  the moving distance is so small that the contact line is considered to be pinned on the B to A boundary. The slow movement of the contact line in X-axis direction causes an increase in  $S'_A$  and a decrease in  $S'_B$ . The characteristic contact angle  $\theta_c$  is also constantly decreasing during the slow movement of the contact line in X-axis direction and  $\theta_c = 105.3^\circ$ ,  $91.8^\circ$  and  $75.45^\circ$ , respectively. When  $\theta_c$  approaches  $\theta_A$ ,  $|\cos \theta_c - \cos \theta_A|$  increases and  $|\cos \theta_c - \cos \theta_B|$  decreases. According to Eq. (23), the unbalanced Young's force on both sides of the B to A boundary achieve dynamic equilibrium. The effective area ( $S'_A$  and  $S'_B$ ) and  $\theta_c$  are related and interact with each other. It is noticed that the constant decrease in  $W_y$  leads to an gradual increase in the curvature of the contact line in X-axis direction. This is why the contact line in X-axis direction moves faster in stage II.

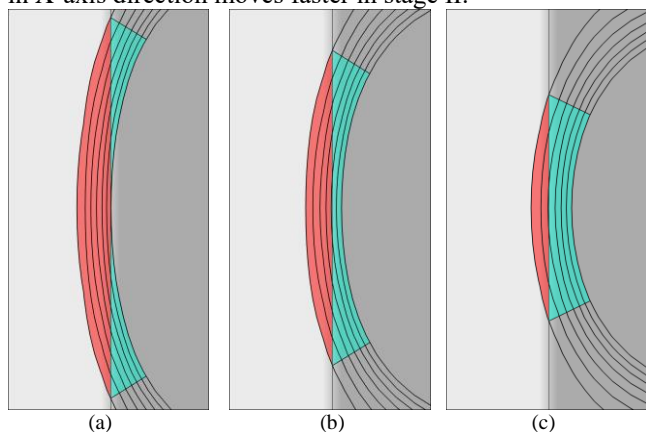


**Fig 10.** Local details of the liquid-vapor interfaces at the contact line during droplet evaporation on the  $W_{11}$  surface: (a)  $t=15800 \delta_t$ , (b)  $t=16200 \delta_t$  and (c)  $t=16600 \delta_t$ .

## 4. CONCLUSIONS

In this work, the modified pseudo-potential lattice Boltzmann model was used to simulate the evaporation of 3D droplet on the chemically stripe-patterned surfaces. The pinning-depinning mechanism of the contact line during droplet evaporation was revealed in 3D space. In particular, a local force balance theory near the stripe boundary was proposed and an equation was formulated to predict the contact angle. The main conclusions are as following:

(1) When the contact line is pinned on the stripe boundary, opposite direction of the local force (unbalanced Young's force) is observed on the hydrophilic and hydrophobic stripe covered by the contact line near the stripe boundary. The local force on the contact line near the stripe boundary is balanced by the self-adjustment of the droplet. The characteristic contact angle of the 3D droplet can be accurately predicted by the equation derived from the local force balance theory.

(2) When the contact line is not pinned on the stripe boundary, the droplet loses the ability of self-adjustment. Once there are disturbances during droplet spreading and evaporation, the force balance on the contact line will be broken, resulting in asymmetric migration of the droplet.

(3) The stick-slip-jump behavior and the CCR-Mixed-CCA mode are clearly observed during the evaporation of the droplets. During the pinning-depinning process, the contact line near the stripe boundary in X-axis direction moves slowly and the local force achieves a dynamic equilibrium. The increasing curvature accelerates the movement of the contact line in X-axis direction until the contact line is detached from the stripe boundary.

This work provides theoretical support for investigating the 3D droplets evaporation on patterned surface.

## AUTHOR INFORMATION

### Corresponding Author

\*E-mail: [jiangx@scut.edu.cn](mailto:jiangx@scut.edu.cn).

### Author Contributions

The manuscript was written through contributions of all authors. All authors have given approval to the final version of the manuscript. † These authors contributed equally.

## ACKNOWLEDGMENT

The project is supported by the National Natural Science Foundation of China (No. 51576070).

## References

- [1] M. Singh, H.M. Haverinen, P. Dhagat, G.E. Jabbour, Inkjet printing—process and its applications, *ADV MATER*, 22 (2010) 673-685.
- [2] E.L. Talbot, L. Yang, A. Berson, C.D. Bain, Control of the particle distribution in inkjet printing through an evaporation-driven sol-gel transition, *ACS APPL MATER INTER*, 6 (2014) 9572-9583.
- [3] W. Cheng, W. Zhang, H. Chen, L. Hu, Spray cooling and flash evaporation cooling: the current development and application, *Renewable and Sustainable Energy Reviews*, 55 (2016) 614-628.
- [4] S. Zhang, Q. Li, I.A. Kinloch, A.H. Windle, Ordering in a droplet of an aqueous suspension of single-wall carbon nanotubes on a solid substrate, *LANGMUIR*, 26 (2009) 2107-2112.
- [5] T. Furuta, M. Sakai, T. Isobe, A. Nakajima, Evaporation behavior of microliter- and sub-nanoliter-scale water droplets on two different fluoroalkylsilane coatings, *LANGMUIR*, 25 (2009) 11998-12001.
- [6] V. Dugas, J. Broutin, E. Souteyrand, Droplet evaporation study applied to DNA chip manufacturing, *LANGMUIR*, 21 (2005) 9130-9136.
- [7] S.T. Chang, O.D. Velev, Evaporation-Induced Particle Microseparations inside Droplets Floating on a Chip, *LANGMUIR*, 22 (2006) 1459-1468.
- [8] N. Miljkovic, R. Enright, Y. Nam, K. Lopez, N. Dou, J. Sack, E.N. Wang, Jumping-droplet-enhanced condensation on scalable superhydrophobic nanostructured surfaces, *NANO LETT*, 13 (2012) 179-187.
- [9] R. Xiao, N. Miljkovic, R. Enright, E.N. Wang, Immersion condensation on oil-infused heterogeneous surfaces for enhanced heat transfer, *SCI REP-UK*, 3 (2013) 1988.

- [10] R. Wen, Q. Li, J. Wu, G. Wu, W. Wang, Y. Chen, X. Ma, D. Zhao, R. Yang, Hydrophobic copper nanowires for enhancing condensation heat transfer, *NANO ENERGY*, 33 (2017) 177-183.
- [11] R. Wang, J. Zhu, K. Meng, H. Wang, T. Deng, X. Gao, L. Jiang, Bio - Inspired Superhydrophobic Closely Packed Aligned Nanoneedle Architectures for Enhancing Condensation Heat Transfer, *ADV FUNCT MATER*, 28 (2018) 1800634.
- [12] Y. Hou, M. Yu, X. Chen, Z. Wang, S. Yao, Recurrent filmwise and dropwise condensation on a beetle mimetic surface, *ACS NANO*, 9 (2014) 71-81.
- [13] I. Kiper, R. Fulcrand, C. Pirat, G. Simon, B. Stutz, S. Ramos, Sessile drop evaporation on (super) hydrophobic surfaces: Effect of low pressure on the contact line dynamics, *Colloids and Surfaces A: Physicochemical and Engineering Aspects*, 482 (2015) 617-623.
- [14] Z. Pan, S. Dash, J.A. Weibel, S.V. Garimella, Assessment of Water Droplet Evaporation Mechanisms on Hydrophobic and Superhydrophobic Substrates, *LANGMUIR*, 29 (2013) 15831-15841.
- [15] Q. Li, P. Zhou, H.J. Yan, Pinning - Depinning Mechanism of the Contact Line during Evaporation on Chemically Patterned Surfaces: A Lattice Boltzmann Study, *LANGMUIR*, 32 (2016) 9389-9396.
- [16] J. Zhang, F. Müller-Plathe, F. Leroy, Pinning of the Contact Line during Evaporation on Heterogeneous Surfaces: Slowdown or Temporary Immobilization? Insights from a Nanoscale Study, *LANGMUIR*, 31 (2015) 7544-7552.
- [17] W.Z. Yuan, L.Z. Zhang, Pinning-Depinning Mechanisms of the Contact Line during Evaporation of Microdroplets on Rough Surfaces: A Lattice Boltzmann Simulation, *Langmuir*, 2018, 34(26): 7906-7915.
- [18] F. Wang, H. Wu, Pinning and depinning mechanism of the contact line during evaporation of nano-droplets sessile on textured surfaces, *SOFT MATTER*, 9 (2013) 573-579.
- [19] H. Kusumaatmaja, J.M. Yeomans, Modeling Contact Angle Hysteresis on Chemically Patterned and Superhydrophobic Surfaces, *LANGMUIR*, 23 (2007) 6019-6032.
- [20] X. Chen, R. Ma, J. Li, C. Hao, W. Guo, B.L. Luk, S.C. Li, S. Yao, Z. Wang, Evaporation of Droplets on Superhydrophobic Surfaces: Surface Roughness and Small Droplet Size Effects, *PHYS REV LETT*, 109 (2012).
- [21] D.I. Yu, H.J. Kwak, S.W. Doh, H.C. Kang, H.S. Ahn, M. Kiyofumi, H.S. Park, M.H. Kim, Wetting and evaporation phenomena of water droplets on textured surfaces, *INT J HEAT MASS TRAN*, 90 (2015) 191-200.
- [22] J.K. Park, J. Ryu, B.C. Koo, S. Lee, K.H. Kang, How the change of contact angle occurs for an evaporating droplet: effect of impurity and attached water films, *SOFT MATTER*, 8 (2012) 11889-11896.
- [23] D. Orejon, K. Sefiane, M.E.R. Shanahan, Stick - Slip of Evaporating Droplets: Substrate Hydrophobicity and Nanoparticle Concentration, *LANGMUIR*, 27 (2011) 12834-12843.
- [24] D. Iwahara, H. Shinto, M. Miyahara, K. Higashitani, Liquid Drops on Homogeneous and Chemically Heterogeneous Surfaces: A Two-Dimensional Lattice Boltzmann Study, *LANGMUIR*, 19 (2003) 9086-9093.
- [25] H.P. Jansen, K. Sotthewes, C. Ganser, H.J. Zandvliet, C. Teichert, E.S. Kooij, Shape of picoliter droplets on chemically striped patterned substrates, *LANGMUIR*, 30 (2014) 11574-81.
- [26] C. Lee, S. Lyu, J.W. Park, W. Hwang, Lattice Boltzmann simulation of the movement of droplets on stripe-patterned surfaces having different wettability, *ADV ENG SOFTW*, 91 (2016) 44-50.
- [27] H.P. Jansen, H.J.W. Zandvliet, E.S. Kooij, Evaporation of elongated droplets on chemically stripe-patterned surfaces, *INT J HEAT MASS TRAN*, 82 (2015) 537-544.
- [28] H. Li, W. Fang, Y. Li, Q. Yang, M. Li, Q. Li, X. Feng, Y. Song, Spontaneous droplets gyrating via asymmetric self-splitting on heterogeneous surfaces, *NAT COMMUN*, 10 (2019).
- [29] S. Varagnolo, D. Ferraro, P. Fantinel, M. Pierno, G. Mistura, G. Amati, L. Biferale, M. Sbragaglia, Stick-slip sliding of water drops on chemically heterogeneous surfaces, *PHYS REV LETT*, 111 (2013) 066101.
- [30] W. Xu, C. Choi, From sticky to slippery droplets: dynamics of contact line depinning on superhydrophobic surfaces, *PHYS REV LETT*, 109 (2012) 024504.
- [31] J.R. Moffat, K. Sefiane, M.E. Shanahan, Effect of TiO<sub>2</sub> nanoparticles on contact line stick - slip behavior of volatile drops, *The Journal of Physical Chemistry B*, 113 (2009) 8860-8866.
- [32] R.G. Picknett, R. Bexon, The evaporation of sessile or pendant drops in still air, *J COLLOID INTERF SCI*, 61 (1977) 336-350.
- [33] D.M. Soolaman, H. Yu, Water microdroplets on molecularly tailored surfaces: correlation between wetting hysteresis and evaporation mode switching, *The Journal of Physical Chemistry B*, 109 (2005) 17967-17973.
- [34] J. Kim, S.I. Ahn, J.H. Kim, W. Zin, Evaporation of water droplets on polymer surfaces, *LANGMUIR*, 23 (2007) 6163-6169.
- [35] Z. Pan, S. Dash, J.A. Weibel, S.V. Garimella, Assessment of water droplet evaporation mechanisms on hydrophobic and superhydrophobic substrates, *LANGMUIR*, 29 (2013) 15831-15841.
- [36] N. Anantharaju, M. Panchagnula, S. Neti, Evaporating drops on patterned surfaces: Transition from pinned to moving triple line, *J COLLOID INTERF SCI*, 337 (2009) 176-182.
- [37] C.W. Extrand, Contact Angles and Hysteresis on Surfaces with Chemically Heterogeneous Islands, *LANGMUIR*, 19 (2003) 3793-3796.
- [38] G. Lichao, T.J. McCarthy, An attempt to correct the faulty intuition perpetuated by the Wenzel and Cassie "laws", *Langmuir the Acs Journal of Surfaces & Colloids*, 25 (2009) 7249-55.
- [39] A. Cassie, Contact angles, *Discussions of the Faraday society*, 3 (1948) 11-16.
- [40] G. Shuai, C. Ping, A lattice Boltzmann method for simulation of liquid - vapor phase-change heat transfer, *International Journal of Heat & Mass Transfer*, 55 (2012) 4923-4927.
- [41] ShuaiGong, PingCheng, Numerical Investigation of Saturated Flow Boiling in Microchannels by the Lattice Boltzmann Method, *Numerical Heat Transfer*, 65 (2014) 644-661.
- [42] S. Gong, P. Cheng, Direct numerical simulations of pool boiling curves including heater's thermal responses and the effect of vapor phase's thermal conductivity, *INT COMMUN HEAT MASS*, 87 (2017) 61-71.
- [43] S. Yi, D. Hang, P.D.M. Spelt, Numerical Simulations of Flows with Moving Contact Lines, *ANNU REV FLUID MECH*, 46 (2017) 97-119.